Time-lapse imaging of bacterial morphology facilitates classification of antimicrobial agents

Xudong Ouyang[1,2], Jelmer Hoeksma[1], Tjalling K. Siersma[3], Leendert W. Hamoen[3] and Jeroen den Hertog[1,2*]

1. Hubrecht Institute-KNAW and University Medical Center Utrecht, Utrecht, the Netherlands
2. Institute Biology Leiden, Leiden University, Leiden, the Netherlands
3. Swammerdam Institute for Life Sciences, University of Amsterdam, Amsterdam, the Netherlands

* Corresponding author, j.denhertog@hubrecht.eu

Running title: Dynamic bacterial morphology imaging

Keywords: bacterial time-lapse imaging, Gram-positive, mechanism of action, antimicrobial, *B. subtilis*

Abstract

Antimicrobial resistance is a major threat to human health. Basic knowledge of antimicrobial mechanism of action (MoA) is imperative for patient care and for identification of novel antimicrobials. However, the process of antimicrobial MoA identification is relatively laborious. Here, we developed a simple, quantitative time-lapse fluorescence imaging method, Dynamic Bacterial Morphology Imaging (DBMI), to facilitate this process. It uses a membrane dye and a nucleoid dye to track the morphological changes of single *Bacillus subtilis* cells in response to antimicrobials for up to 60 min. DBMI of bacterial cells facilitated assignment of the MoAs of 14 distinct, known antimicrobial compounds to the five main classes. Using this method, we found that the poorly studied antimicrobial, harzianic acid, a secondary metabolite that we purified from the fungal culture of *Oidiodendron flavum*, targets the cell envelope. We conclude that DBMI is a simple method, which facilitates rapid classification of the MoA of antimicrobials in functionally distinct classes.

32 **Introduction**

33 As the number of untreatable infections caused by multidrug-resistant “superbugs” is
34 increasing globally, antimicrobial resistance is becoming a major threat to human health
35 (Hancock, 2005; Blair et al., 2015). New antimicrobials with distinct working mechanisms
36 are required to combat bacteria that have become resistant to all known antimicrobials.
37 Although thousands of small molecules have now been screened for antibacterial activity in
38 countless screening programs, the yield of useful compounds from these is relatively low
39 (Payne et al., 2007). One of the reasons is the lack of insight into antimicrobial mechanism
40 of action (MoA), which makes it difficult to determine the value of a new compound.
41 Therefore, understanding the MoA is fundamental for identification of novel antimicrobials.

42 Transcriptomic and proteomic technologies have been developed to assess the MoA of
43 antimicrobial agents in recent years (Van Duy et al., 2007; Silver, 2011). Transcriptomic
44 analyses generate information about the expression of genes in response to antimicrobials
45 (Pulido et al., 2016) and provide transcriptome-wide overviews of gene expression and are
46 therefore used at the initial stages of target identification. Proteomic approaches generate
47 overviews of protein levels, and changes in response to antimicrobial treatment may provide
48 insight into the working mechanism (Brötz-Oesterhelt et al., 2005; Armengaud, 2013).
49 Whereas these methods provide valuable information about antimicrobial targets, they do
50 not necessarily provide information about the direct target(s) of antimicrobials. Because the
51 time spent and cost involved in the genetic and omics-approaches is relatively high, they
52 are not the best approaches for initial stages of target identification. A simple, cost-effective

53 method would be preferred as a first approach.

54 Recently, imaging-based approaches started to be applied for antimicrobial MoA
55 prediction. Bacterial cytological profiling was developed for Gram-negative bacteria to
56 classify antimicrobial agents, utilizing high resolution fluorescent microscopy of cells stained
57 with fluorescent dyes, or expressing fluorescent reporters (Nonejuie et al., 2013; Sun et al.,
58 2018). For Gram-positive bacteria, a panel of GFP reporters was developed, covering many
59 pathways and this panel was used successfully for in-depth analysis of antimicrobial targets
60 (Müller et al., 2016; Wenzel et al., 2018; Zhu et al., 2018). Here, we developed a method to
61 rapidly distinguish the effect of anti-Gram-positive bacterial compounds from all of the five
62 main target classes, cell membrane, cell wall, protein, DNA or RNA. To achieve this, we
63 used time-lapse imaging of fluorescent dye-stained *B. subtilis* to record dynamic changes.
64 We improved the imaging protocol to make it simple and functional for bacterial long-term
65 imaging. Using this method, dubbed Dynamic Bacterial Morphology Imaging (DBMI), we
66 observed bacteria over time and established fluorescence intensities qualitatively and
67 quantitatively. It allowed to rapidly distinguish between antimicrobials from all of the five
68 different classes. Finally, we purified an antimicrobial activity from the fungal culture of
69 *Oidiodendron flavum* and identified it to be harzianic acid, an understudied fungal secondary
70 metabolite. Using DBMI, we established that harzianic acid targets the cell membrane and
71 cell wall.

72

73 **Materials and Methods**

74 *Strains and reagents*

75 *B. subtilis* 168 was used for imaging in this study (Kunst et al., 1997). *O. flavum* (CBS
76 366.71) was obtained from Westerdijk Fungal Biodiversity Institute (the Netherlands) and
77 used for biologically active compound production. Commercial antimicrobials were
78 purchased from Sigma Aldrich (Table 1). FM4-64, 4′,6-diamidino-2-phenylindole (DAPI),
79 SYTO-9 and SYTOX-Green were purchased from Thermo Fisher Scientific.

80

81 *Microdilution assay*

82 MIC (Minimum Inhibitory Concentration) was determined by broth microdilution assay.
83 Early exponential-phase cultures of *B. subtilis* were diluted 1:100 into Luria-Bertani (LB)
84 medium, and distributed in 96-wells plates. Antimicrobials were tested 1:10 of the stock, then
85 serially diluted with a factor 2. Bacterial growth was visually inspected after overnight
86 incubation at 37 °C.

87

88 *Confocal microscopy*

89 Microscopy was performed as described before with minor modification (Müller et al.,
90 2016). Briefly, bacterial cultures in early exponential-phase were treated with antimicrobials
91 (2.5 × MIC) or 1% dimethyl sulfoxide (DMSO) as control for up to 60 min. Afterwards, 1.5
92 μM FM4-64 was used for membrane staining. 5 μM DAPI, 50 nM SYTO-9 or 0.5 μM SYTOX-

93 Green was applied to stain nucleoids. Samples were then immobilized on microscope slides
94 covered with an agarose pad containing 1% agarose and LB medium, and imaged. Confocal
95 microscopy was carried out using a Perkin Elmer UltraView VoX spinning disk microscope
96 system and Volocity v6.3 software. Z-stack images were collected over a length of 3 μm with
97 0.2 μm intervals to acquire signals from the whole cells. Three independent experiments
98 were done using each antimicrobial (biological triplicates). Images were analyzed using Fiji
99 (Schindelin et al., 2012).

100

101 *Time-lapse microscopy*

102 A single well agarose pad (2 mL in size) containing 0.75% agarose, 1.5 μM FM4-64, 50
103 nM SYTO-9 and LB medium was made by a trimmed syringe to immobilize bacterial cells
104 on its surface. Bacterial culture in early exponential-phase was treated with 1.5 μM FM4-64
105 and 25 nM SYTO-9 for 10 min, and then 5 μL of it was transferred onto the agarose pad for
106 imaging. Time-lapse images were collected using the spinning disk microscope system
107 described above for 30 to 60 min with 3 min intervals. 400 μL LB medium with antimicrobials
108 (2.5 × MIC) or 1% DMSO (control) was added into the well on the agarose pad after the
109 second image was taken to make sure the cells were growing normally. Images were
110 analyzed using Fiji.

111

112 DBMI *patterns*

113 Stack images were merged by Z projection using max intensity and cell morphological
114 patterns were measured by Fiji. A wide line (width: 20-pixel, i.e. 1.3 μm) was drawn to cover
115 a whole cell and the intensity of both membrane signal and nucleoid signal over the line was
116 acquired with the tool Plot Profile. The graphs of Plot Profile from each series of time-lapse
117 imaging were then re-plotted into one heatmap with GraphPad Prism v8.4.1 to generate the
118 DBMI patterns.

119

120 *Analysis of DBMI images*

121 Stack images were merged by Z projection using max intensity. One cell unit was
122 defined as a cell without any septa shown in the image of the initial time point. Cell status
123 analysis was done by counting cells by eye in each of the three cell type categories (intact
124 cell, no-nucleoid cell and disintegrated cell). Cell morphology analysis was done by
125 measuring the length and intensity of both membrane and nucleoid using Fiji. Bar graphs
126 and line chart were plotted using GraphPad Prism v8.4.1.

127

128 *Identification of biologically active compound*

129 *O. flavum* was cultured on Malt Extract Agar (MEA) for 14 days. Secondary metabolites
130 were extracted using ethyl acetate and separated using a Shimadzu preparative high
131 performance liquid chromatography (HPLC) system with a C18 reversed phase Reprosil
132 column (10 μm, 120 Å, 250 × 22 mm). The mobile phase was 0.1% trifluoroacetic acid in

133 water (buffer A) and 0.1% trifluoroacetic acid in acetonitrile (buffer B). A linear gradient was
134 applied of buffer B (5–95%) for 40 minutes. Fractions were collected and tested on *B. subtilis.*
135 The active fraction was assessed for its purity through Shimadzu LC-2030 analytical HPLC
136 using a Shimadzu Shim-pack GISTC18-HP reversed phase column (3 µm, 4.6 × 100 mm).
137 LC-MS was performed on a Shimadzu LC-system connected to a Bruker Daltonics µTOF-
138 Q mass spectrometer. High resolution mass spectrometry (HRMS) was measured on an
139 LCT instrument (Micromass Ltd, Manchester UK). Elemental composition analyses were
140 performed by Mikroanalytisch Labor Kolbe (Oberhausen, Germany). Finally, the compound
141 was dissolved in 400 µL $CDCl_3$ + 0,03% TMS and analyzed by Nuclear Magnetic Resonance
142 (NMR) spectroscopy. More specifically, ^{1}H-NMR, Hetronuclear Single Quantum Coherence
143 (HSQC), Hetronuclear Multile-Bond Correlation (HMBC) and Correlation spectroscopy
144 (COSY) spectra were measured at 600 MHz using a Bruker instrument. ^{13}C-NMR was
145 measured on the same instrument at 150 MHz.
146

147 **Results**

148 *Static morphological differences did not fully distinguish the effect of antimicrobials on*
149 *bacteria*

150 Most antimicrobials for Gram-positives fall into one of five main classes based on their
151 MoA: cell membrane, cell wall, protein, DNA or RNA (Peach et al., 2013). We set out to use
152 morphological differences to distinguish MoAs between different classes of antimicrobials
153 against Gram-positive bacteria. To this end, we selected one antimicrobial from each class.
154 *B. subtilis* was treated for 60 min with the antimicrobials using 2.5 × MIC (Table 1) to ensure
155 the inhibitory effects. The cells were stained with FM4-64 (red, cell membrane) and DAPI
156 (blue, nucleoid), immobilized and imaged. Ampicillin (cell wall class) treatment for 60 min
157 did not alter the appearance of cells compared to control treatment (Fig. 1). The other four
158 antimicrobials induced variations both with respect to membrane and nucleoid staining. On
159 the membrane, bright fluorescent foci appeared in response to all four antimicrobials,
160 suggesting that the cytoskeleton was affected (Strahl et al., 2014). However, similar foci
161 were also sometimes observed in the control, precluding the presence of foci as a criterion
162 to distinguish between antimicrobial classes. Nucleoid staining was divided into two groups:
163 decondensed nucleoids in response to CCCP (cell membrane class) and rifampin (RNA
164 class), and shorter, more condensed nucleoids in response to moxifloxacin (DNA class) and
165 chloramphenicol (protein class). In addition, the nucleoid dye SYTOX-Green was applied
166 separately to check the permeability of cells. However, no cells were shown to have
167 permeable membrane in response to CCCP or ampicillin (Fig. S1A). Taken together,

168 analysis of membrane and nucleoid staining of immobilized cells after treatment with
169 antimicrobials for 60 min was not sufficient to definitively distinguish between the five classes
170 of antimicrobials. Nevertheless, some differences were observed and we hypothesized that
171 the response over time might be distinct. To investigate the dynamics of the cells' responses
172 to antimicrobials, we set up time-lapse imaging of bacteria stained with fluorescent dyes.

173

174 *DBMI distinguished antimicrobials from distinct MoA classes*

175 To acquire dynamic morphological patterns, SYTO-9 was used as nucleoid dye. We also
176 designed the following workflow to enable time-lapse imaging of bacteria(Fig. 2). Images
177 were taken every three minutes to prevent cells from laser damage, and two images were
178 acquired before antimicrobials were added to confirm that the bacteria were growing
179 healthily. To facilitate quantitative dynamic imaging of individual cells, the fluorescence
180 intensity was integrated and quantified along the length of the cell and plotted. Control cells
181 treated with DMSO showed steady growth over the course of 60 min (Fig. 3). DBMI was
182 initially performed with the same antimicrobials as in the static bacterial imaging experiment.
183 Images were collected for 60 min and resulting movies are shown in Movie S1-S6.

184 Cells treated with different classes of antimicrobials had notably distinct profiles. The
185 ampicillin and CCCP profiles stood out, because the nucleoid fluorescence signals suddenly
186 became almost undetectable (Fig. 3). Ampicillin treatment inhibited cell growth and
187 subsequently, the nucleoid fluorescence was lost. Strikingly, the membrane fluorescence at
188 the septum started to decrease a few minutes after cell growth was inhibited. Part of the

189 membrane fluorescence was lost at the end of the imaging series, showing that cells treated
190 with ampicillin disintegrated, which was also evident from the actual micrograph (Fig. 3D).
191 In response to CCCP, the membrane pattern remained normal. However, the nucleoid
192 fluorescence intensity decreased sharply already after 6 min of treatment and cells stopped
193 growing at the same time. The apparent loss of SYTO-9 staining was unexpected, because
194 CCCP-treatment did not significantly affect DAPI-stained nucleoids (Fig. 1). Double labeling
195 of nucleoids with SYTO-9 and DAPI showed that CCCP-treatment for 3 min already greatly
196 reduced the SYTO-9 signal. In high contrast, SYTO-9 was still detectable. Yet, DAPI labeling
197 appeared not to be affected in the same CCCP-treated cells (Fig. 4). Similar results were
198 obtained after CCCP-treatment for 60 min (Fig. S1B). These results indicate that rapid
199 reduction in SYTO-9 labeling of nucleoids was not due to loss of nucleoids from the cells,
200 but rather to loss of SYTO-9 fluorescence.

201 Chloramphenicol and moxifloxacin induced shorter nucleoids relative to the cell size (Fig.
202 3), but the dynamics were different. In chloramphenicol treated cells, the extension of
203 nucleoids was totally arrested, and the nucleoids compacted, resulting in an apparent
204 increase in space between the nucleoids. In moxifloxacin-treated cells, the nucleoids still
205 extended, but slower than the cells themselves, resulting in an increase in the space
206 between nucleoids. Rifampin induced the nucleoid signal to gradually spread over the cells,
207 suggesting that the nucleoids decondensed, which is in line with previous studies (Chen et
208 al., 1996; Bakshi et al., 2015). Taken together, these results suggest that DBMI distinguished
209 the MoA of antimicrobials from five major classes.

210

211 *Rapid loss of nucleoid staining was distinct in cells treated with antimicrobials from cell*
212 *membrane and cell wall classes*

213 In order to determine whether the DBMI profiles were conserved in each class, we tested
214 14 distinct antimicrobials from the five main antimicrobial classes (Table 1) using DBMI. All
215 the profiles were first analyzed by eye for nucleoid visibility and membrane integrity to derive
216 cell status, which was featured into three types: intact cells, having both visible membrane
217 and nucleoid fluorescence; no-nucleoid cells, intact cells without visible nucleoid
218 fluorescence; and disintegrated cells, no detectable nucleoid fluorescence and a
219 disintegrated membrane. Cell status was evaluated over time to determine the changes in
220 the ratios of each cell type during treatment.

221 As expected, antimicrobials within the cell membrane class (triclosan, nisin and CCCP)
222 and the cell wall class (ampicillin, penicillin G and vancomycin) showed distinct profiles by
223 cell status analysis and were readily distinguished from the other three classes (Fig. 5A,
224 S1C). The percentage of intact cells decreased strongly after treatment with antimicrobials
225 from the cell membrane and cell wall classes, compared to the other three classes. However,
226 some antimicrobials from RNA and protein classes, including rifampin, gentamicin and
227 chloramphenicol, also induced loss of nucleoid fluorescence in a small proportion of the cells
228 (Fig. S1C). Quantification of nucleoid intensity of individual cells over time indicated that
229 rifampin, gentamicin and chloramphenicol treatment resulted in gradual loss of nucleoid
230 intensity (Fig. S1D). In contrast, treatment with cell membrane-active and cell wall-active

231 antimicrobials resulted in a sharp decrease of nucleoid fluorescence intensity in each
232 individual cell (Fig. 5B). Next, to distinguish the classes further, quantitative analysis of the
233 changes in the membrane fluorescence intensity, cell length and the nucleoid length was
234 done over time. Differences in membrane appearance and nucleoid shape were also
235 recorded.

236 To distinguish the cell membrane class from the cell wall class, we evaluated the
237 percentage of intact cells (Fig. 5A) and the inhibition of cell growth (Fig. 5C). Cell wall-active
238 antimicrobial treatment induced loss of nucleoid fluorescence and inhibition of cell growth
239 after 15 - 30 min of treatment. Cell wall-active antimicrobials also induced disintegration of
240 cells within 12 min after losing nucleoid fluorescence. Disintegrated cells were only observed
241 upon treatment with cell wall-active antimicrobials, making this both a unique and a
242 conserved trait for this class. In contrast, cell membrane-active antimicrobials induced
243 simultaneous arrest of cell growth and loss of nucleoid fluorescence at an early stage of the
244 antimicrobial treatment. These results indicate that the loss of nucleoid fluorescence is the
245 first effect of cell membrane-active antimicrobials and distinguishes the class of cell
246 membrane-active antimicrobials from the other classes. Like for CCCP, co-staining of
247 nucleoids using SYTO-9 and DAPI indicated that loss of SYTO-9 fluorescence was not
248 caused by loss of nucleoids themselves (Fig. S1E). Taken together, DBMI facilitates the
249 distinction between cell wall and cell membrane active antimicrobials.

250 Next, we assessed differences between the cells treated with the three non-envelope-
251 associated classes of antimicrobials. Since most of the cells remained intact during

252 treatment (Fig. S1C), we investigated the potential differences in cell morphology, first
253 focusing on changes in nucleoid length (Fig. 6A, S1F) in comparison with changes in cell
254 length (Fig. 5C, 6B). To visualize this comparison, the ratio between nucleoid length and cell
255 length was calculated (Fig. S1G). If not detectable, the nucleoid length was recorded as 0
256 µm. In response to cell wall and cell membrane active antimicrobials, nucleoid fluorescence
257 was lost abruptly. In contrast, the two antimicrobials from the RNA class (rifampin and
258 actinomycin D) induced an increase in nucleoid length compared to cell length, albeit with
259 different dynamics. This indicated that an increased ratio of nucleoid length to cell length
260 was conserved following treatment with antimicrobials from the RNA class, which is
261 consistent with a previous report about nucleoid compaction (Cabrera et al., 2009). In
262 comparison, treatment with antimicrobials from both the DNA class (moxifloxacin, mitomycin
263 C and nalidixic acid) and the protein class (chloramphenicol, fusidic acid and gentamicin)
264 reduced nucleoid length compared to cell length (Fig. S1G). For cells treated with
265 antimicrobials from the protein class, nucleoid elongation stopped immediately, suggesting
266 DNA elongation was blocked shortly after the antimicrobial was added. Since cell growth
267 was not totally inhibited (fusidic acid) or was inhibited more slowly than the inhibition of
268 nucleoid growth (chloramphenicol and gentamicin), the ratio of nucleoid length to cell length
269 was reduced. The antimicrobials from the DNA class did not inhibit nucleoid elongation
270 completely, but reduced it to some extent. Additionally, during treatment, the separation of
271 nucleoids seemed to be poorly controlled and unusual shapes of nucleoids were often
272 observed (e.g. Fig. 7A at 30 min), in line with known effects of these antimicrobials on DNA
273 replication (Sugino et al., 1977; Drlica and Zhao, 1997; Paz et al., 2012). Hence, each class

274 of antimicrobials we tested generated a unique and reproducible DBMI profile.

275

276 *DBMI distinguished sub-classes within the cell membrane, cell wall and RNA classes*

277 Subsequently, we investigated whether DBMI was also able to distinguish sub-classes
278 within the five main classes. In the cell membrane class, the growth curve of nisin-treated
279 cells was notable, showing stabilized and even decreased cell size when the drug was
280 added (Fig. 5C), which might due to loss of turgor pressure. In addition, big membrane blobs
281 were observed after loss of nucleoid intensity at 30 min (Fig. 7B). Triclosan and CCCP
282 generated highly similar profiles, but there was still a detectable morphological difference
283 between the treated cells at 30 min (Fig. 7B). CCCP did not induce effects on the membrane,
284 whereas triclosan induced small fluorescent membrane foci. These results are in line with
285 their MoAs: nisin generates pores in the membrane, whereas triclosan and CCCP destroy
286 membrane polarization, albeit at different levels (Kasianowicz et al., 1984; Russell, 2004;
287 Prince et al., 2016). This indicates that DBMI may be used to distinguish between cell
288 membrane-active antimicrobials.

289 When comparing the profiles within the cell wall class, vancomycin was found to
290 generate a different profile than ampicillin and penicillin G. The cell growth inhibition in
291 response to vancomycin was delayed by 20 min compared to the other two (Fig. 5C). Before
292 cell growth inhibition at 30 min, some fluorescent blobs were detected on the membrane,
293 indicating membrane aggregates during vancomycin treatment, which is distinct from cells
294 treated with ampicillin or penicillin G (Fig. 7B). Ampicillin and penicillin G generated similar

295 DBMI profiles and they both inhibit cross linking of peptidoglycans (Williamson et al., 1980),
296 whereas vancomycin affects lipid II synthesis (Boger, 2001). Thus, we conclude that DBMI
297 is able to distinguish antimicrobials of the cell wall class.

298 Rifampin of the RNA class induced rapid elongation of the nucleoid whereas cell length
299 was almost constant, resulting in an increase in nucleoid length: cell length ratio (Fig. 6A, B
300 and S1G), indicating that the nucleoids in these cells were decondensed (Cabrera et al.,
301 2009) and almost fully filled the cells (Fig. 7A). Although the increase in the ratio of nucleoid
302 length to cell length was also observed in actinomycin D treated cells, it was much slower
303 than in rifampin treated cells, suggesting that actinomycin D has a different target to block
304 RNA synthesis, which is consistent with previous reports (Wehrli, 1983; Sobell, 1985).

305 Next, we explored differences of the profiles of antimicrobial treatments within the
306 protein class and the DNA class. Whereas most of the dynamic changes were similar among
307 the three selected antimicrobials of the protein class, changes in nucleoid intensity were
308 distinct for each antimicrobial (Fig. S1D). None of the fusidic acid treated cells showed a
309 reduction in nucleoid intensity, whereas half of the chloramphenicol treated cells and all of
310 the gentamicin treated cells showed a decrease in nucleoid intensity. This might be related
311 to their different MoAs (Dobie and Gray, 2004; Borovinskaya et al., 2007; Siibak et al., 2009),
312 but the large variability in nucleoid intensities in chloramphenicol treated cells precluded
313 nucleoid intensity as a good parameter to distinguish between antimicrobials within the
314 protein category. For the DNA class of antimicrobials, the responses were too similar to
315 distinguish between them.

316 Taken together, DBMI facilitated distinction between antimicrobials from the five main
317 classes, and allowed to distinguish sub-classes within the cell membrane, cell wall and RNA
318 classes, using the scheme, depicted in Fig. 8.

319

320 *Identification of Harzianic Acid*

321 Previously, we screened fungal metabolites from more than 10,000 fungi for bioactive
322 compounds (Hoeksma et al., 2019). Here, we screened this library for antimicrobial activity
323 against Gram-positive bacteria (*S. aureus*). One of the fungi, *O. flavum* (CBS 366.71),
324 produced high antimicrobial activity. The active compound was purified and the chemical
325 characteristics (Table 2, Fig. S2) were consistent with data previously reported for harzianic
326 acid (Sawa et al., 1994; Vinale et al., 2014) (Fig. 9A).

327 Harzianic acid: $C_{19}H_{27}NO_6$, dark yellow powder. HRMS: found 388.1750 (M+Na),
328 calculated 388.1736 for $C_{19}H_{27}NO_6Na$. Elemental composition analyses: C 61,4%; O 21,8%;
329 H 7,0%; N 3,8%. NMR (600 MHz, $CDCl_3$): See Table 2. UV-Vis λ_{max}: 244 nm, 363 nm.

330

331 *MoA Identification of Harzianic Acid*

332 Little is known about harzianic acid, a compound with antimicrobial activity that was
333 isolated from fungi decades ago (Sawa et al., 1994). Harzianic acid also has antifungal
334 activity and plant growth promoting activity (Vinale et al., 2009, 2014; De Filippis et al., 2020;
335 De Tommaso et al., 2020). The antimicrobial MoA of harzianic acid is unknown. DBMI was

336 used to get insight into the MoA of harzianic acid. Imaging data were analyzed to assess
337 cell status and cell morphology (Fig. 9B, S1). Harzianic acid induced loss of nucleoid
338 fluorescence at an early stage of treatment. Cell growth was totally inhibited at an early
339 stage as well. This was reminiscent of the initial action of cell membrane-active
340 antimicrobials. Cell length actually appeared to decrease when the drug was added,
341 suggesting loss of turgor pressure. Big membrane aggregates were observed when intact
342 cells lost their nucleoid fluorescence, i.e. from 9 min onwards (Movie S7). These effects
343 were similar to the effects of nisin, suggesting that harzianic acid generated pores in the
344 membrane. Cell status data also indicated that part of the cells disintegrated. Note the gaps
345 along the membrane at 30 min (Fig. 9C) or from 18 min onwards (Movie S7). Whereas
346 disintegrated membranes were evident in nisin-treated cells as previously shown in static
347 bacterial imaging (Lamsa et al., 2012), we did not observe disintegrated cells in response to
348 nisin by DBMI up to 30 min treatment. Disintegration of part of the cells in response to
349 harzianic acid may therefore suggest that harzianic acid also partially affects the cell wall.

350 The final disintegrated cell membrane showed similarities to the cell membrane of
351 vancomycin treated cells, but the dynamics suggested that pore formation in the membrane
352 was the initial effect of harzianic acid. To investigate this, non-cell permeable SYTOX Green
353 was used to stain nucleoids. Evidently, treatment with harzianic acid or nisin, but not
354 vancomycin or vehicle control (DMSO) induced SYTOX Green staining of the nucleoid (Fig.
355 9D). In conclusion, harzianic acid generated pores in the membrane and eventually
356 appeared to affect the cell wall.

357 **Discussion**

358 Here we used time-lapse imaging of live, stained Gram-positive bacteria to rapidly
359 distinguish the MoA classes of antimicrobial agents. In order to acquire dynamic profiles of
360 bacteria under different conditions, we used SYTO-9 instead of DAPI, because DAPI is toxic
361 to bacterial cells. SYTO-9 shows low bacterial toxicity, fast staining, high fluorescence
362 intensity in the green spectrum and therefore good compatibility with FM4-64 fluorescence.
363 We also developed an imaging protocol (Fig. 2), which is based on a previously described
364 technique (de Jong et al., 2011). A thick agarose pad provides enough nutrition to sustain
365 cell growth and the well on top of the agarose is convenient for adding antimicrobial solutions
366 to bacteria at any stage of the imaging process. In addition, the preparation is fast because
367 no fridge-cool-down or precision-work steps are required. Using this imaging technique,
368 which we called DBMI, we are able to reliably predict the MoA of antimicrobials at three
369 levels (Fig. 8).

370 At the first level, antimicrobials were divided into two groups, based on whether they
371 exert their effect on the cell envelope or not. All of the inhibitors that induce cell envelope
372 stress induced a sudden loss of SYTO-9 nucleoid fluorescence, which is distinct from the
373 effects of antimicrobials with non-cell-envelope stress targets. Rapid loss of SYTO-9 staining
374 might be caused by sudden changes in intracellular milieu due to a compromised cell
375 envelope, which affects SYTO-9 fluorescence. Which environmental factor(s) affect SYTO-
376 9 fluorescence, be it membrane potential, pH, ionic profile or osmolarity, remains to be
377 determined (Auty et al., 2001; Stiefel et al., 2015).

378 At the next level, antimicrobials were further distinguished into five distinct classes. For
379 antimicrobials from the cell membrane class, cell growth arrest and loss of nucleoid staining
380 occurred simultaneously, which was not observed in cells treated with cell wall active
381 antimicrobials. In addition, cell wall active antimicrobials led to disintegrated cells eventually,
382 which is presumably due to the decrease in peptidoglycan synthesis and increase in
383 autolysins (Kohanski et al., 2010). Interestingly, this pattern was not observed in static
384 bacterial imaging, e.g. ampicillin treated cells in Fig. 1. This discrepancy is likely caused by
385 the different imaging methods that were used. Time lapse imaging of the same cell showed
386 disintegration of the cell (Fig. 3D), whereas treatment in liquid medium for 60 min and
387 subsequent transfer for imaging may cause disintegrated cells to go unnoticed and only
388 intact cells are imaged (Fig. 1). The non-cell-envelope associated antimicrobials from
389 different classes did not induce sudden loss of nucleoid fluorescence. Cells treated with RNA
390 synthesis inhibitors showed decondensed nucleoids, whereas antimicrobials affecting the
391 protein or DNA class both induced compacted nucleoids, consistent with earlier reports
392 (Bylund et al., 1993; Van Helvoort et al., 1996; Bakshi et al., 2015). Unusual nucleoid shapes
393 and shorter nucleoids may be due to a DNA segregation block and/or dissected nucleoids
394 by division (Georgopapadakou and Bertasso, 1991; Chen et al., 1996; Drlica et al., 2008).

395 At the third level, antimicrobials from cell membrane, cell wall and RNA classes were
396 further distinguished into sub-classes. In the cell membrane class, the appearance of the
397 membrane seemed to be related to the extent of the permeability. From CCCP to triclosan
398 to nisin, the permeability increased and apparently, so did the extent of the membrane

399 aggregation. Notable among them was triclosan, which has multiple targets in the cytoplasm
400 and membrane. High concentrations of triclosan have bactericidal effects and are mediated
401 by membrane targets (Russell, 2004). Here, we used high concentrations (2.5 × MIC), which
402 had bactericidal effects. DBMI classified triclosan in the cell membrane class, which is
403 consistent with bactericidal concentrations of triclosan acting on membrane targets. In the
404 cell wall class, vancomycin binds to different target groups than the penicillins (Williamson
405 et al., 1980; Boger, 2001), which is in line with the observed aggregation of membrane only
406 in response to vancomycin in the cell wall class. In the RNA category, due to the differences
407 in targets (Wehrli, 1983; Sobell, 1985), the extent of decondensing of nucleoids was shown
408 to be different. Inhibiting RNA polymerase by rifampin might affect RNA synthesis faster than
409 actinomycin D binding to DNA at the transcription initiation complex, resulting in totally
410 decondensed nucleoids in rifampin treated cells and only partially decondensed nucleoids
411 in actinomycin D treated cells.

412

413

414 **Conclusion**

415 DBMI facilitates profiling of changes over time in cell morphology and viability. With the
416 obtained parameters, antimicrobials may be classified at three levels. DBMI does not require
417 prior knowledge of the antimicrobial MoAs. Hence, DBMI may be used to rapidly distinguish
418 the MoA class and subclass of known and unknown antimicrobials.

Acknowledgements

The authors would like to thank Anko de Graaff of the Hubrecht Imaging Centre for help with imaging, and Samantha van der Beek and Maja Solman for help with developing the imaging protocol. This project was supported by the Chinese Scholarship Council (CSC).

424 **References**

425 Armengaud, J. (2013). Microbiology and proteomics, getting the best of both worlds! *Environ.*
426 *Microbiol.* 15, 12–23. doi:10.1111/j.1462-2920.2012.02811.x.

427 Auty, M. A. E., Gardiner, G. E., McBrearty, S. J., O'Sullivan, E. O., Mulvihill, D. M., Collins,
428 J. K., et al. (2001). Direct in situ viability assessment of bacteria in probiotic dairy
429 products using viability staining in conjunction with confocal scanning laser microscopy.
430 *Appl. Environ. Microbiol.* 67, 420–425. doi:10.1128/AEM.67.1.420-425.2001.

431 Bakshi, S., Choi, H., and Weisshaar, J. C. (2015). The spatial biology of transcription and
432 translation in rapidly growing Escherichia coli. *Front. Microbiol.* 6, 1–15.
433 doi:10.3389/fmicb.2015.00636.

434 Blair, J. M. A., Webber, M. A., Baylay, A. J., Ogbolu, D. O., and Piddock, L. J. V. (2015).
435 Molecular mechanisms of antibiotic resistance. *Nat. Rev. Microbiol.* 13, 42–51.
436 doi:10.1038/nrmicro3380.

437 Boger, D. L. (2001). Vancomycin, teicoplanin, and ramoplanin: Synthetic and mechanistic
438 studies. *Med. Res. Rev.* 21, 356–381. doi:10.1002/med.1014.

439 Borovinskaya, M. A., Pai, R. D., Zhang, W., Schuwirth, B. S., Holton, J. M., Hirokawa, G., et
440 al. (2007). Structural basis for aminoglycoside inhibition of bacterial ribosome recycling.
441 *Nat. Struct. Mol. Biol.* 14, 727–732. doi:10.1038/nsmb1271.

442 Brötz-Oesterhelt, H., Bandow, J. E., and Labischinski, H. (2005). Bacterial proteomics and
443 its role in antibacterial drug discovery. *Mass Spectrom. Rev.* 24, 549–565.

444 doi:10.1002/mas.20030.

445 Bylund, J. E., Haines, M. A., Piggot, P. J., and Higgins, M. L. (1993). Axial filament formation
446 in Bacillus subtilis: Induction of nucleoids of increasing length after addition of
447 chloramphenicol to exponential-phase cultures approaching stationary phase. *J.*
448 *Bacteriol.* 175, 1886–1890. doi:10.1128/jb.175.7.1886-1890.1993.

449 Cabrera, J. E., Cagliero, C., Quan, S., Squires, C. L., and Ding, J. J. (2009). Active
450 transcription of rRNA operons condenses the nucleoid in Escherichia coli: Examining
451 the effect of transcription on nucleoid structure in the absence of transertion. *J. Bacteriol.*
452 191, 4180–4185. doi:10.1128/JB.01707-08.

453 Chen, C. R., Malik, M., Snyder, M., and Drlica, K. (1996). DNA gyrase and topoisomerase
454 IV on the bacterial chromosome: Quinolone-induced DNA cleavage. *J. Mol. Biol.* 258,
455 627–637. doi:10.1006/jmbi.1996.0274.

456 De Filippis, A., Nocera, F. P., Tafuri, S., Ciani, F., Staropoli, A., Comite, E., et al. (2020).
457 Antimicrobial activity of harzianic acid against Staphylococcus pseudintermedius. *Nat.*
458 *Prod. Res.* 0, 1–6. doi:10.1080/14786419.2020.1779714.

459 de Jong, I. G., Beilharz, K., Kuipers, O. P., and Veening, J. W. (2011). Live cell imaging of
460 Bacillus subtilis and Streptococcus pneumoniae using automated time-lapse
461 microscopy. *J. Vis. Exp.*, 1–6. doi:10.3791/3145.

462 De Tommaso, G., Salvatore, M. M., Nicoletti, R., DellaGreca, M., Vinale, F., Bottiglieri, A., et
463 al. (2020). Bivalent metal-chelating properties of harzianic acid produced by

464 Trichoderma pleuroticola associated to the gastropod Melarhaphe neritoides.
465 *Molecules* 25. doi:10.3390/molecules25092147.

466 Dobie, D., and Gray, J. (2004). Fusidic acid resistance in Staphylococcus aureus. *Arch. Dis.*
467 *Child.* 89, 74–77. doi:10.1136/adc.2003.019695.

468 Drlica, K., Malik, M., Kerns, R. J., and Zhao, X. (2008). Quinolone-mediated bacterial death.
469 *Antimicrob. Agents Chemother.* 52, 385–392. doi:10.1128/AAC.01617-06.

470 Drlica, K., and Zhao, X. (1997). DNA gyrase, topoisomerase IV, and the 4-quinolones.
471 *Microbiol. Mol. Biol. Rev.* 61, 377–392. doi:10.1128/.61.3.377-392.1997.

472 Georgopapadakou, N. H., and Bertasso, A. (1991). Effects of quinolones on nucleoid
473 segregation in Escherichia coli. *Antimicrob. Agents Chemother.* 35, 2645–2648.
474 doi:10.1128/AAC.35.12.2645.

475 Hancock, R. E. W. (2005). Mechanisms of action of newer antibiotics for Gram-positive
476 pathogens. *Lancet Infect. Dis.* 5, 209–218. doi:10.1016/S1473-3099(05)70051-7.

477 Hoeksma, J., Misset, T., Wever, C., Kemmink, J., Kruijtzer, J., Versluis, K., et al. (2019). A
478 new perspective on fungal metabolites: identification of bioactive compounds from fungi
479 using zebrafish embryogenesis as read-out. *Sci. Rep.* 9, 1–16. doi:10.1038/s41598-
480 019-54127-9.

481 Kasianowicz, J., Benz, R., and McLaughlin, S. (1984). The kinetic mechanism by which
482 CCCP (carbonyl cyanide m-Chlorophenylhydrazone) transports protons across
483 membranes. *J. Membr. Biol.* 82, 179–190. doi:10.1007/BF01868942.

484 Kohanski, M. A., Dwyer, D. J., and Collins, J. J. (2010). How antibiotics kill bacteria: From
485 targets to networks. *Nat. Rev. Microbiol.* 8, 423–435. doi:10.1038/nrmicro2333.

486 Kunst, F., Ogasawara, N., Moszer, I., Albertini, A. M., Alloni, G., Azevedo, V., et al. (1997).
487 The complete genome sequence of the gram-positive bacterium Bacillus subtilis.
488 *Nature* 390, 249–256. doi:10.1038/36786.

489 Lamsa, A., Liu, W. T., Dorrestein, P. C., and Pogliano, K. (2012). The Bacillus subtilis
490 cannibalism toxin SDP collapses the proton motive force and induces autolysis. *Mol.*
491 *Microbiol.* 84, 486–500. doi:10.1111/j.1365-2958.2012.08038.x.

492 Müller, A., Wenzel, M., Strahl, H., Grein, F., Saaki, T. N. V., Kohl, B., et al. (2016). Daptomycin
493 inhibits cell envelope synthesis by interfering with fluid membrane microdomains. *Proc.*
494 *Natl. Acad. Sci. U. S. A.* 113, E7077–E7086. doi:10.1073/pnas.1611173113.

495 Nonejuie, P., Burkart, M., Pogliano, K., and Pogliano, J. (2013). Bacterial cytological profiling
496 rapidly identifies the cellular pathways targeted by antibacterial molecules. *Proc. Natl.*
497 *Acad. Sci. U. S. A.* 110, 16169–16174. doi:10.1073/pnas.1311066110.

498 Payne, D. J., Gwynn, M. N., Holmes, D. J., and Pompliano, D. L. (2007). Drugs for bad bugs:
499 Confronting the challenges of antibacterial discovery. *Nat. Rev. Drug Discov.* 6, 29–40.
500 doi:10.1038/nrd2201.

501 Paz, M. M., Zhang, X., Lu, J., and Holmgren, A. (2012). A new mechanism of action for the
502 anticancer drug Mitomycin C: Mechanism-based inhibition of thioredoxin reductase.
503 *Chem. Res. Toxicol.* 25, 1502–1511. doi:10.1021/tx3002065.

504 Peach, K. C., Bray, W. M., Winslow, D., Linington, P. F., and Linington, R. G. (2013).
505 Mechanism of action-based classification of antibiotics using high-content bacterial
506 image analysis. *Mol. Biosyst.* 9, 1837–1848. doi:10.1039/c3mb70027e.

507 Prince, A., Sandhu, P., Kumar, P., Dash, E., Sharma, S., Arakha, M., et al. (2016). Lipid-II
508 Independent Antimicrobial Mechanism of Nisin Depends on Its Crowding and Degree
509 of Oligomerization. *Sci. Rep.* 6, 1–15. doi:10.1038/srep37908.

510 Pulido, M. R., García-Quintanilla, M., Gil-Marqués, M. L., and McConnell, M. J. (2016).
511 Identifying targets for antibiotic development using omics technologies. *Drug Discov.*
512 *Today* 21, 465–472. doi:10.1016/j.drudis.2015.11.014.

513 Russell, A. D. (2004). Whither triclosan? *J. Antimicrob. Chemother.* 53, 693–695.
514 doi:10.1093/jac/dkh171.

515 Sawa, R., Mori, Y., Iinuma, H., Naganawa, H., Hamada, M., Yoshida, S., et al. (1994).
516 Harzianic acid, a new antimicrobial antibiotic from a fungus. *J. Antibiot. (Tokyo).* 47,
517 731–732. doi:10.7164/antibiotics.47.731.

518 Schindelin, J., Arganda-Carreras, I., Frise, E., Kaynig, V., Longair, M., Pietzsch, T., et al.
519 (2012). Fiji: An open-source platform for biological-image analysis. *Nat. Methods* 9,
520 676–682. doi:10.1038/nmeth.2019.

521 Siibak, T., Peil, L., Xiong, L., Mankin, A., Remme, J., and Tenson, T. (2009). Erythromycin-
522 and chloramphenicol-induced ribosomal assembly defects are secondary effects of
523 protein synthesis inhibition. *Antimicrob. Agents Chemother.* 53, 563–571.

524 doi:10.1128/AAC.00870-08.

525 Silver, L. L. (2011). Challenges of antibacterial discovery. *Clin. Microbiol. Rev.* 24, 71–109.
526 doi:10.1128/CMR.00030-10.

527 Sobell, H. M. (1985). Actinomycin and DNA transcription. *Proc. Natl. Acad. Sci. U. S. A.* 82,
528 5328–5331. doi:10.1073/pnas.82.16.5328.

529 Stiefel, P., Schmidt-Emrich, S., Maniura-Weber, K., and Ren, Q. (2015). Critical aspects of
530 using bacterial cell viability assays with the fluorophores SYTO9 and propidium iodide.
531 *BMC Microbiol.* 15, 1–9. doi:10.1186/s12866-015-0376-x.

532 Strahl, H., Bürmann, F., and Hamoen, L. W. (2014). The actin homologue MreB organizes
533 the bacterial cell membrane. *Nat. Commun.* 5, 1–11. doi:10.1038/ncomms4442.

534 Sugino, A., Peebles, C. L., Kreuzer, K. N., and Cozzarelli, N. R. (1977). Mechanism of action
535 of nalidixic acid: Purification of Escherichia coli nalA gene product and its relationship
536 to DNA gyrase and a novel nicking-closing enzyme. *Proc. Natl. Acad. Sci. U. S. A.* 74,
537 4767–4771. doi:10.1073/pnas.74.11.4767.

538 Sun, Y., Heidary, D. K., Zhang, Z., Richards, C. I., and Glazer, E. C. (2018). Bacterial
539 Cytological Profiling Reveals the Mechanism of Action of Anticancer Metal Complexes.
540 *Mol. Pharm.* 15, 3404–3416. doi:10.1021/acs.molpharmaceut.8b00407.

541 Van Duy, N., Mäder, U., Tran, N. P., Cavin, J. F., Tam, L. T., Albrecht, D., et al. (2007). The
542 proteome and transcriptome analysis of Bacillus subtilis in response to salicylic acid.
543 *Proteomics* 7, 698–710. doi:10.1002/pmic.200600706.

544 Van Helvoort, J. M. L. M., Kool, J., and Woldringh, C. L. (1996). Chloramphenicol causes
545 fusion of separated nucleoids in Escherichia coli K-12 cells and filaments. *J. Bacteriol.*
546 178, 4289–4293. doi:10.1128/jb.178.14.4289-4293.1996.

547 Vinale, F., Flematti, G., Sivasithamparam, K., Lorito, M., Marra, R., Skelton, B. W., et al.
548 (2009). Harzianic acid, an antifungal and plant growth promoting metabolite from
549 Trichoderma harzianum. *J. Nat. Prod.* 72, 2032–2035. doi:10.1021/np900548p.

550 Vinale, F., Manganiello, G., Nigro, M., Mazzei, P., Piccolo, A., Pascale, A., et al. (2014). A
551 novel fungal metabolite with beneficial properties for agricultural applications.
552 *Molecules* 19, 9760–9772. doi:10.3390/molecules19079760.

553 Wehrli, W. (1983). Rifampin: Mechanisms of action and resistance. *Rev. Infect. Dis.* 5, S407–
554 S411. doi:10.1093/clinids/5.Supplement_3.S407.

555 Wenzel, M., Rautenbach, M., Vosloo, J. A., Siersma, T., Aisenbrey, C. H. M., Zaitseva, E., et
556 al. (2018). The multifaceted antibacterial mechanisms of the pioneering peptide
557 antibiotics tyrocidine and gramicidin S. *MBio* 9, 1–20. doi:10.1128/mBio.00802-18.

558 Williamson, R., Hakenbeck, R., and Tomasz, A. (1980). In vivo interaction of β-lactam
559 antibiotics with the penicillin-binding proteins of Streptococcus pneumoniae. *Antimicrob.*
560 *Agents Chemother.* 18, 629–637. doi:10.1128/AAC.18.4.629.

561 Zhu, J. H., Wang, B. W., Pan, M., Zeng, Y. N., Rego, H., and Javid, B. (2018). Rifampicin
562 can induce antibiotic tolerance in mycobacteria via paradoxical changes in rpoB
563 transcription. *Nat. Commun.* 9. doi:10.1038/s41467-018-06667-3.

564

565

566 **Table 1. List of antimicrobials used in this study**

Class	Sub-class	Antimicrobials	MIC* (mg/L)	Mode of Action
Cell wall	Penicillin	Ampicillin	5	Binding to Penicillin-binding protein (Williamson et al., 1980)
	Penicillin	Penicillin G	5	Binding to Penicillin-binding protein (Williamson et al., 1980)
	Glycopeptide	Vancomycin	0.25	Binding to D-Ala-D-Ala moiety of peptidoglycan (Boger, 2001)
Cell membrane	Proton ionophore	CCCP	0.4	Transporting protons across membranes (Kasianowicz et al., 1984)
	Polychloro phenoxy phenols	Triclosan	2.5	Disrupting cellular ionic homeostasis at bactericidal concentration (Russell, 2004)
	Lantibiotics	Nisin	2.5	Generating pores on cell membrane (Prince et al., 2016)
Protein	Amphenicols	Chloramphenicol	2.5	Inhibiting the peptidyl transferase activity (Siibak et al., 2009)
	Fusidanes	Fusidic acid	0.13	Binding to the elongation factor G (EF-G) (Dobie and Gray, 2004)
	Aminoglycoside	Gentamicin	2.5	Binding to the A-site on the 16S ribosomal RNA (Borovinskaya et al., 2007)
DNA	Quinolone	Moxifloxacin	0.05	Inhibiting DNA gyrase A and topoisomerase IV (Drlica and Zhao, 1997)
	Quinolone	Nalidixic acid	1.5	Inhibiting DNA gyrase A and topoisomerase IV (Sugino et al., 1977)
	Mitomycin	Mitomycin C	0.06	Cross-linking and alkylating of DNA (Paz et al., 2012)
RNA	Rifamycin	Rifampin	0.13	Inhibiting bacterial RNA polymerase (Wehrli, 1983)
	Actinomycines	Actinomycin D	0.03	Inhibiting bacterial RNA synthesis by binding to DNA at the transcription initiation complex (Sobell, 1985)
Unknown	Harzianic acid	Harzianic acid	50	Unknown

567 * Determined by our stain of *Bacillus subtilis* 168 in this study.

568

569 **Table 2: Assignments NMR-shifts, HMBC and COSY couplings for harzianic acid (in**

570 **$CDCl_3$)**

		Harzianic acid ($CDCl_3$)		
#	**δC[a]**	**δH[b]**	**HMBC[b]**	**COSY[b]**
1	13.7	0.95 (t), 3H	2, 3	2
2	21.8	1.50 (m), 2H	1, 3, 4	1, 3
3	35.5	2.24 (dd), 2H	1, 2, 4, 5	3, 4 or 5[c]
4	149.9	6.37[c] (m), 1H	2, 3, 5, 6, 7[c]	3, 6[c]
5	129.6	6.38[c] (m), 1H	2, 3, 6, 7[c]	3, 6[c]
6	147.6	7.55 (m), 1H	4, 5, 7, 8	4 or 5[c], 7
7	119.1	7.00 (d, *J*=15.1 Hz), 1H	5, 6, 8, 10	6
8	176.7	-	-	-
9	173.2	-	-	-
10	99.7	-	-	-
11	197.3	-	-	-
12	64.1	3.63 (dd, *J*= 10.6, 1,0 Hz), 2H	9, 11, 13, 14, 18,	13
13	33.8	1.89 (dd), 1H 2.48 (d), 1H	11, 12, 14, 15, 19	12
14	79.9	-	-	-
15	36.0	2.02 (m), 1H	13, 14, 16, 17, 19	16 or 17[c]
16	17.5	0.99[c] (m), 3H	14, 15[c]	15
17	16.2	0.99[c] (m), 3H	14, 15[c]	15
18	26.6	2.97 (s), 3H	9, 12	-
19	176.3	-	-	-

571 [a]= measured at 150 MHz, [b]= measured at 600 MHz, [c]= overlapping signals

572

573 **Figure Legends**

574 **Fig. 1. Cytological profiling of antimicrobial activities.** *B. subtilis* cells were treated with
575 an antimicrobial from one of the five main MoA classes or 1% DMSO (control) for 60 min.
576 The antimicrobials we selected were: ampicillin for cell wall, CCCP for cell membrane,
577 chloramphenicol for protein, moxifloxacin for DNA and rifampin for RNA. The concentrations
578 of antimicrobials were 2.5 × MIC. Cells were stained with FM4-64 (red, cell membrane) and
579 DAPI (blue, nucleoid), immobilized and imaged by confocal fluorescence microscopy.
580 Representative images are shown. Scale bar is 5 μm.

581

582 **Fig. 2. Workflow for time-lapse imaging of bacteria.** A single well LB agarose pad was
583 made using a trimmed syringe to immobilize bacterial cells on its surface. A glass slide was
584 used to keep the agarose surface flat and smooth. Upon solidification of the agarose, the
585 glass slide was removed and drops with bacterial cultures were added onto the surface.
586 Once the drops were dry, the agarose pad with bacteria was transferred into a confocal dish
587 for imaging. The thick agarose pad provided enough nutrition to sustain growing cells,
588 allowing time-lapse imaging for hours, even overnight. The well on top of the agarose pad
589 was used for easy addition of antimicrobial solutions to bacteria at any stage of the imaging
590 process. After imaging, raw micrographs were converted into dynamic patterns by
591 quantifying the fluorescence intensities of the membrane and nucleoid staining separately
592 along the length of the bacteria.

593

594 **Fig. 3. Distinct DBMI patterns of cells upon antimicrobial treatments.** *B. subtilis* cells
595 were treated with antimicrobials (2.5 × MIC) as indicated or 1% DMSO (control). The
596 antimicrobials we selected were: ampicillin for cell wall, CCCP for cell membrane,
597 chloramphenicol for protein, moxifloxacin for DNA and rifampin for RNA. Cells were stained
598 with FM4-64 (red, cell membrane) and SYTO-9 (green, nucleoid) and imaged by time lapse
599 confocal fluorescence microscopy for 60 min with 3 min intervals. Column A and D show the
600 actual micrographs of the first and the last picture of the series (contrast was adjusted for
601 individual graph to show details). The FM4-64 (column B) and SYTO-9 (column C) signals
602 in a single cell (arrow in micrographs) were quantified over the length of the cell and plotted
603 (y-axis, numbers in μm) over time (x-axis, numbers in min). Representative cells are shown.
604 Scale bar is 5 μm.

605

606 **Fig. 4. Dual nucleoid staining of cells following CCCP treatment for 3 min.** *B. subtilis*
607 cells were treated with CCCP (2.5 × MIC) or 1% DMSO (control) for 3 min. Cells were stained
608 with FM4-64 (red, cell membrane), SYTO-9 (green, nucleoid) and DAPI (blue, nucleoid),
609 immobilized and imaged by confocal fluorescence microscopy. Representative images are
610 shown. Scale bar is 5 μm. SYTO-9 graphs were shown both in normal contrast and high
611 contrast (HC).

612

613 **Fig. 5. DBMI of cells treated with antimicrobials from the cell membrane and cell wall**
614 **classes.** *B. subtilis* cells were treated with antimicrobials (2.5 × MIC) as indicated or 1%

615 DMSO (control). Cells were stained with FM4-64 (red, cell membrane) and SYTO-9 (green,
616 nucleoid), and imaged by time lapse confocal fluorescence microscopy with 3 min intervals.
617 Three distinct cell types were identified: intact cells (cells with visible membrane and
618 nucleoid fluorescence), no-nucleoid cells (cells with apparently intact membrane, but without
619 visible nucleoid fluorescence), and disintegrated cells (cells with disintegrated membrane
620 and no detectable nucleoid). The number of cells of the three types were counted from
621 biological triplicate imaging series (n > 40). In-depth cell morphology analysis was done on
622 9 cells in total per condition, i.e. 3 cells per biological triplicate. The cell length and nucleoid
623 intensity data were quantified in these cells at each timepoint. (A) The number of cells in
624 each cell type, intact cells (green), no-nucleoid cells (yellow) and disintegrated cells (red),
625 was determined and plotted as percentage (y-axis, numbers in %) over time (x-axis, min).
626 (B) Overall nucleoid intensity, i.e. the SYTO-9 fluorescence intensity inside a whole cell,
627 corrected for background, was determined for individual cells over time and was depicted
628 as percentage of the value at the start (t = 0 min) (y-axis) over time (x-axis, min). The mean
629 of antimicrobial-treated cells was plotted in black with error bars representing the SEM. Gray
630 lines represent individual antimicrobial-treated cells on which the mean was based. (C) Cell
631 length was determined using the membrane signal (FM4-64) and was represented as
632 percentage, relative to the initial length (y-axis, numbers in %) over time (x-axis, min). The
633 mean of antimicrobial-treated cells was plotted in black with error bars representing the SEM.
634 Gray lines represent individual antimicrobial-treated cells on which the mean was based.

635

636 **Fig. 6. DBMI of cells treated with antimicrobials from the DNA, RNA and protein**
637 **classes.** *B. subtilis* cells were treated with antimicrobials (2.5 × MIC) as indicated or 1%
638 DMSO (control). Cells were stained with FM4-64 (red, cell membrane) and SYTO-9 (green,
639 nucleoid), and imaged by time lapse confocal fluorescence microscopy with 3 min intervals.
640 Cell morphology data were analyzed from biological triplicate imaging series in triplicate,
641 hence from 9 cells in total per antimicrobial and processed as described in the legend to Fig.
642 5. Nucleoid length, i.e. the length of all the nucleoids inside one cell added together, is shown
643 in (A) and cell length in (B). In case nucleoid fluorescence was not detectable, the nucleoid
644 length was recorded as 0 µm. The mean of antimicrobial-treated cells was plotted in black
645 with error bars representing the SEM. Gray lines represent individual antimicrobial-treated
646 cells on which the mean was based. DMSO control is depicted in Fig. 5C.

647

648 **Fig. 7. Cell membrane and nucleoid staining of cells after 0 min and 30 min treatment**
649 **with different antimicrobials**. Cells treated with antimicrobials from DNA, RNA and protein
650 class are in (A) and from cell membrane, cell wall classes and DMSO control are in (B).
651 Special patterns induced by moxifloxacin, nalidixic acid, mitomycin C, triclosan and
652 vancomycin are indicated by arrow heads. Representative images are shown. Scale bar is
653 5 µm.

654

655

656 **Fig. 8. Schematic representation of the DBMI-guided antimicrobial MoA identification.**
657 Green boxes indicate well-identified categories or mechanisms, whereas red ones indicate
658 not well-identified. DBMI distinguishes antimicrobial MoAs at three levels. Briefly, *B. subtilis*
659 cells were treated with antimicrobials and imaged. At the first level, based on the loss of
660 nucleoid staining, every antimicrobial was grouped into cell-envelope associated stress or
661 non-cell-envelope associated stress. If the nucleoid staining was suddenly lost, they would
662 fall into cell-envelope stress group. At the second level, five main MoA classes were
663 identified. For the group of cell-envelope stress, if growth inhibition and loss of nucleoid
664 staining occurred simultaneously, cell membrane was supposed to be affected. If growth
665 inhibition occurred before loss of nucleoid staining, cell wall was determined to be affected
666 if disintegrated cells were observed. For the group of non-cell-envelope associated stress,
667 the changing of nucleoid length / cell length ratio before loss of nucleoid staining were
668 measured. If the ratio was becoming larger during imaging, RNA synthesis was supposed
669 to be affected. If the ratio was becoming smaller, the nucleoid growth had to be checked. If
670 DNA elongation was inhibited, the antimicrobial would fall into protein class; if not, into DNA
671 class. At the third level, sub-classes would be identified within cell membrane, cell wall and
672 RNA classes. Protein and DNA classes could not be further distinguished because the
673 differences within these classes were not evident. For the cell membrane class, if cells
674 became shorter and large membrane aggregates were observed, probably pores were
675 generated in the cell membrane. If there were little or no membrane blobs, the cellular ionic
676 homeostasis was supposed to be disrupted. To further distinguish within cell wall class, we
677 looked back to the time before growth inhibition. If cells were normal, the cross linking of

678 peptidoglycans, which was the last step of cell wall synthesis, might be affected. If thicker
679 membrane septa or big membrane blobs were observed, lipid II synthesis might be affected.
680 For the RNA class, the extent of nucleoid decondensing was different between different
681 targets. If RNA polymerase was targeted, nucleoids would be totally decondensed. If
682 transcription complex was affected, the decondensing of nucleoids would be gentler.

683

684 **Fig. 9. MoA identification of harzianic acid.** (A) Chemical structure of harzianic acid. (B)
685 Analysis of DBMI images of harzianic acid. *B. subtilis* cells were treated with harzianic acid
686 (2.5 × MIC). Cells were stained, imaged, analyzed and plotted as in Fig. 5. (C) Examples of
687 micrographs of cells at 0 min, 9 min and 30 min that were used for the quantifications in (B).
688 Disintegrated cells at 30 min are indicated by arrow heads. DMSO treated cells are shown
689 as control. Representative images are shown. Scale bar is 5 μm. (D) Cell permeability assay.
690 *B. subtilis* cells were treated with antimicrobials (2.5 × MIC) or 1% DMSO (control) for 60
691 min. Cells were stained with FM4-64 (red, cell membrane) and SYTOX-Green (green,
692 nucleoid), and imaged by confocal fluorescence microscopy. Representative images are
693 shown. Scale bar is 5 μm.

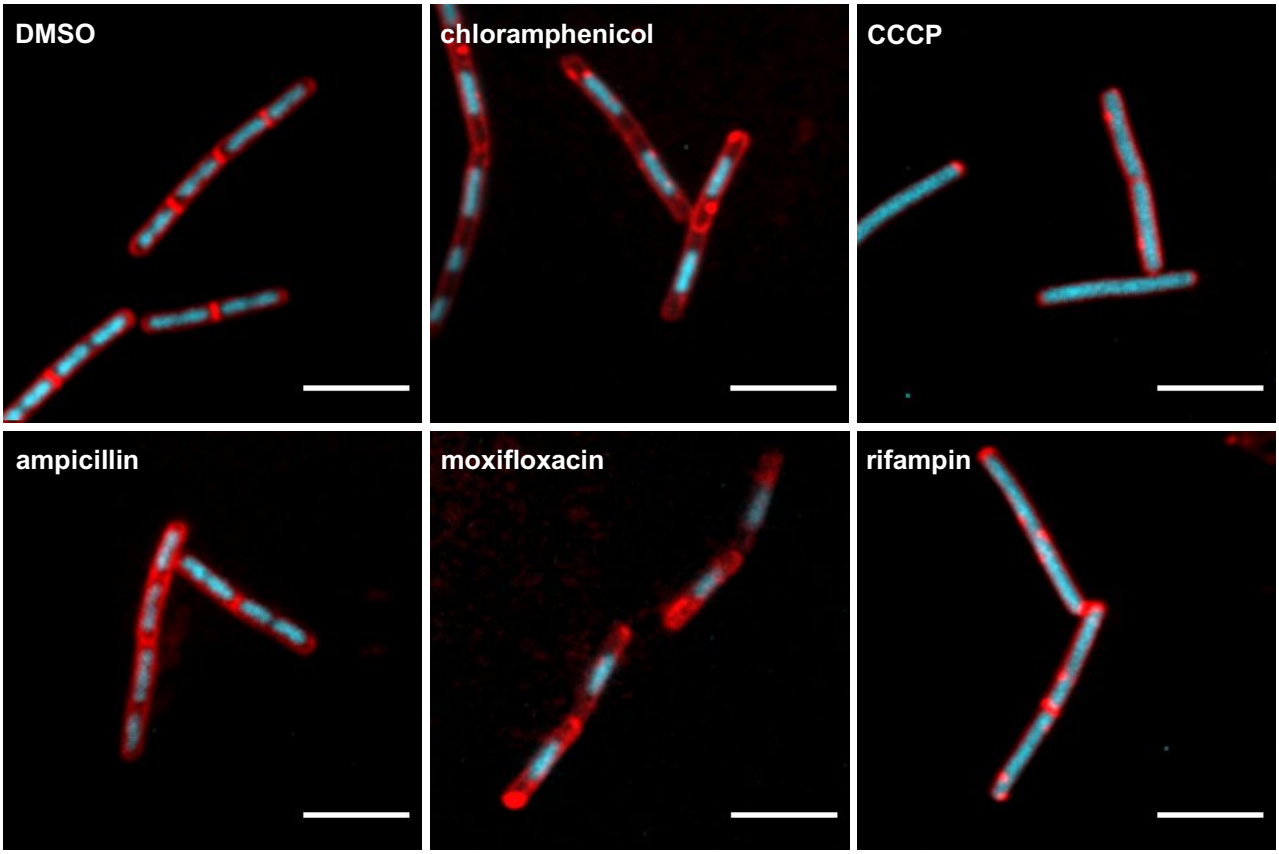
DMSO
chloramphenicol
CCCP
ampicillin
moxifloxacin
rifampin

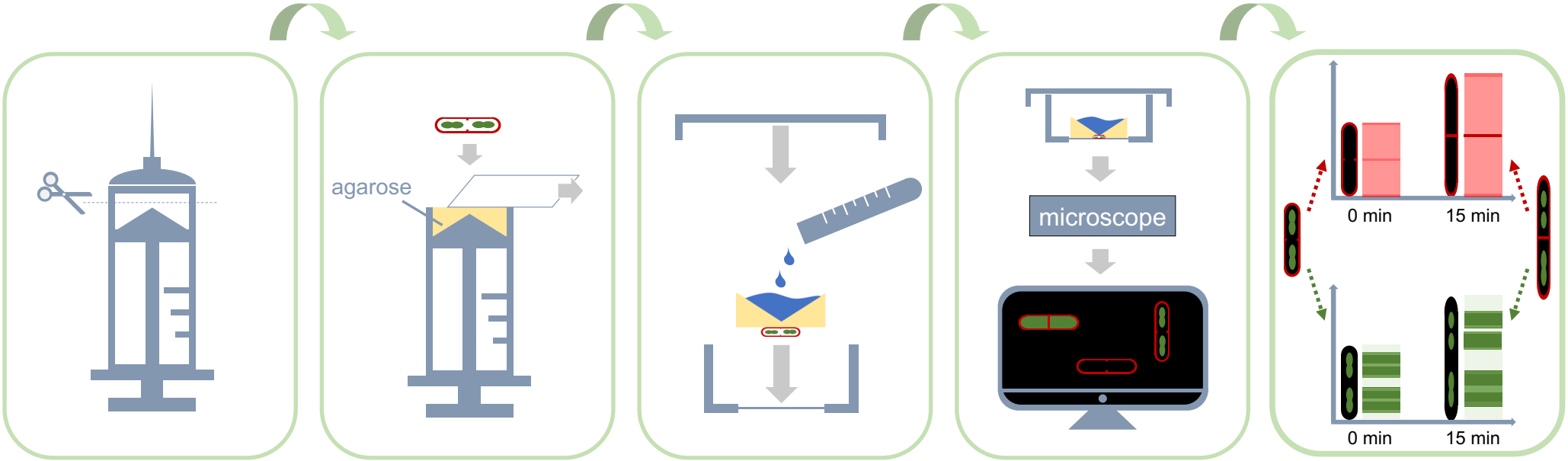
agarose
microscope
0 min
15 min
0 min
15 min

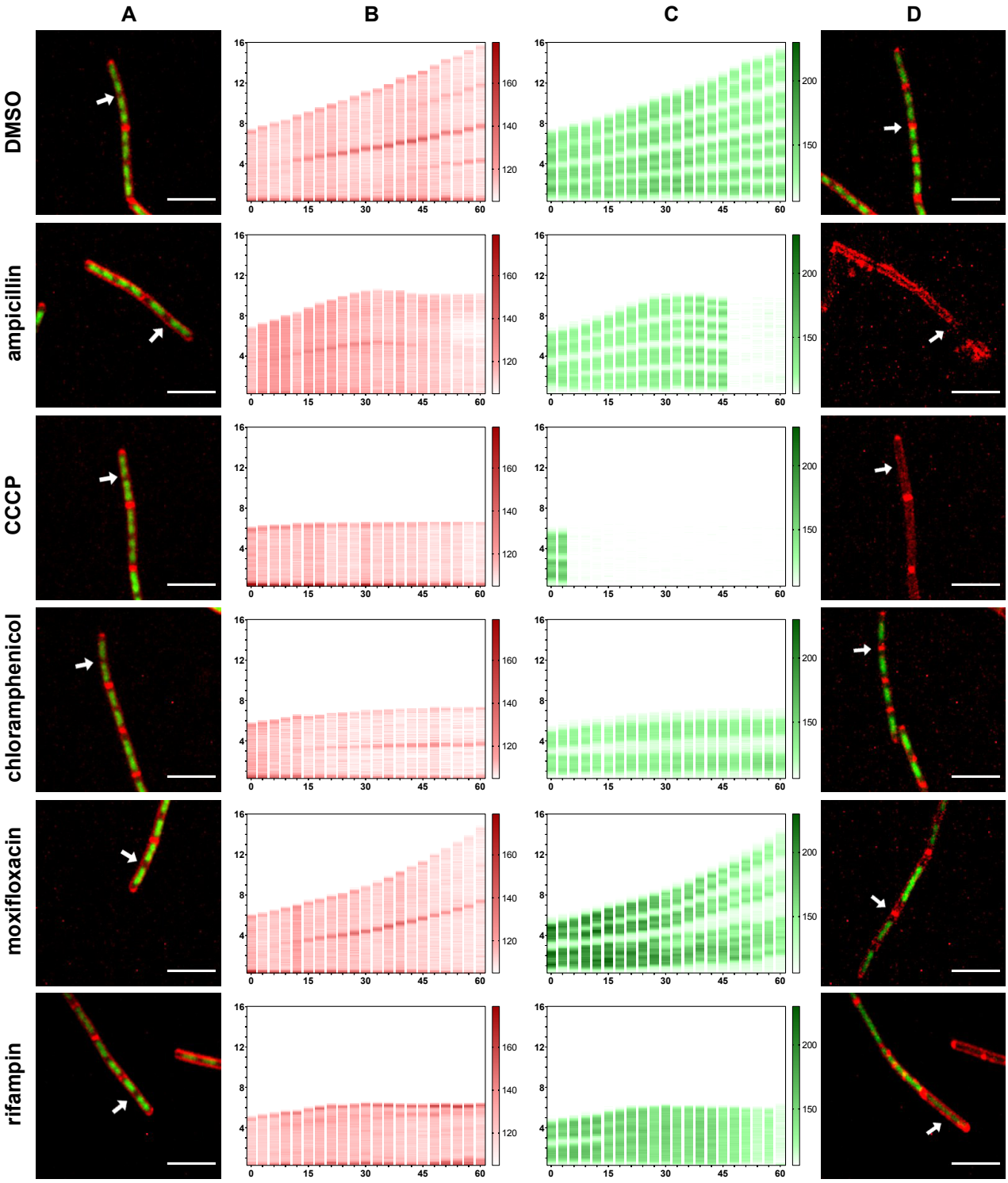
A
B
C
D
DMSO
ampicillin
CCCP
chloramphenicol
moxifloxacin
rifampin
16
12
8
4
0
15
30
45
60
160
140
120
200
150

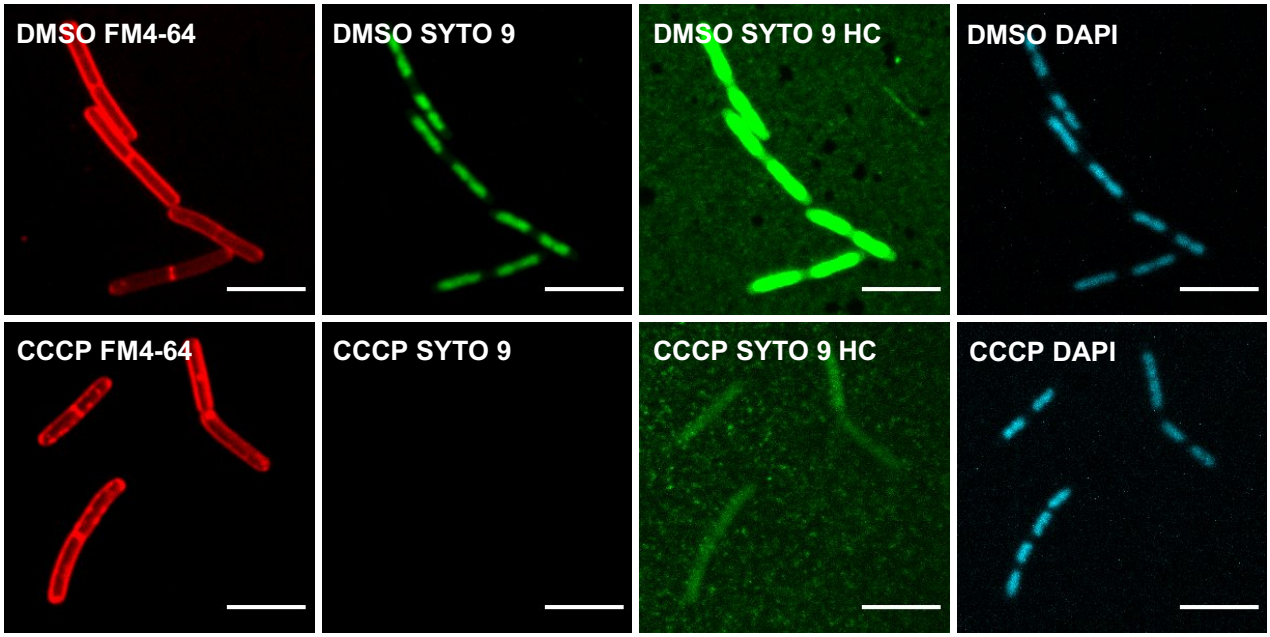
DMSO FM4-64
DMSO SYTO 9
DMSO SYTO 9 HC
DMSO DAPI
CCCP FM4-64
CCCP SYTO 9
CCCP SYTO 9 HC
CCCP DAPI

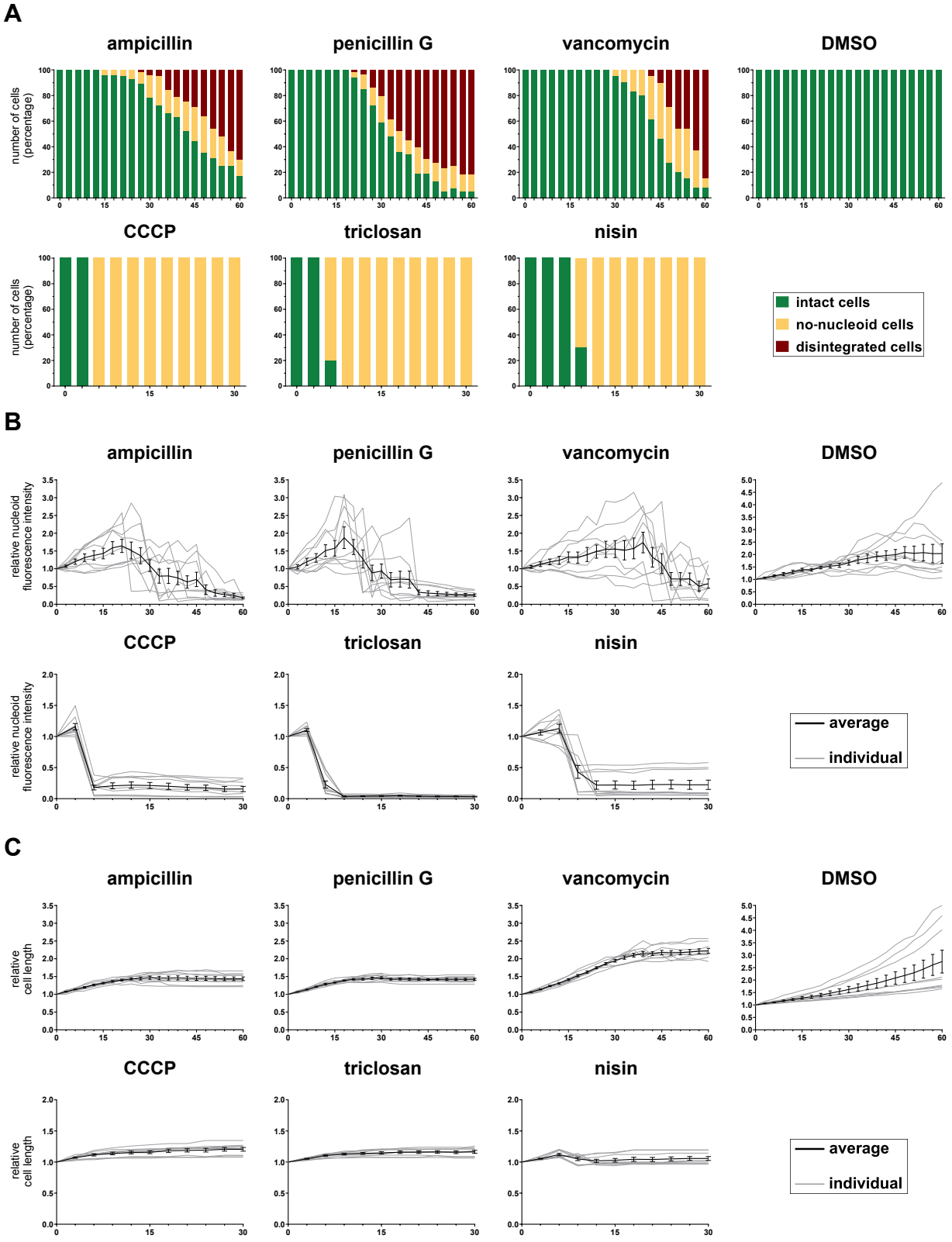
A
ampicillin
penicillin G
vancomycin
DMSO
CCCP
triclosan
nisin
number of cells (percentage)
intact cells
no-nucleoid cells
disintegrated cells
B
relative nucleoid fluorescence intensity
average
individual
C
relative cell length

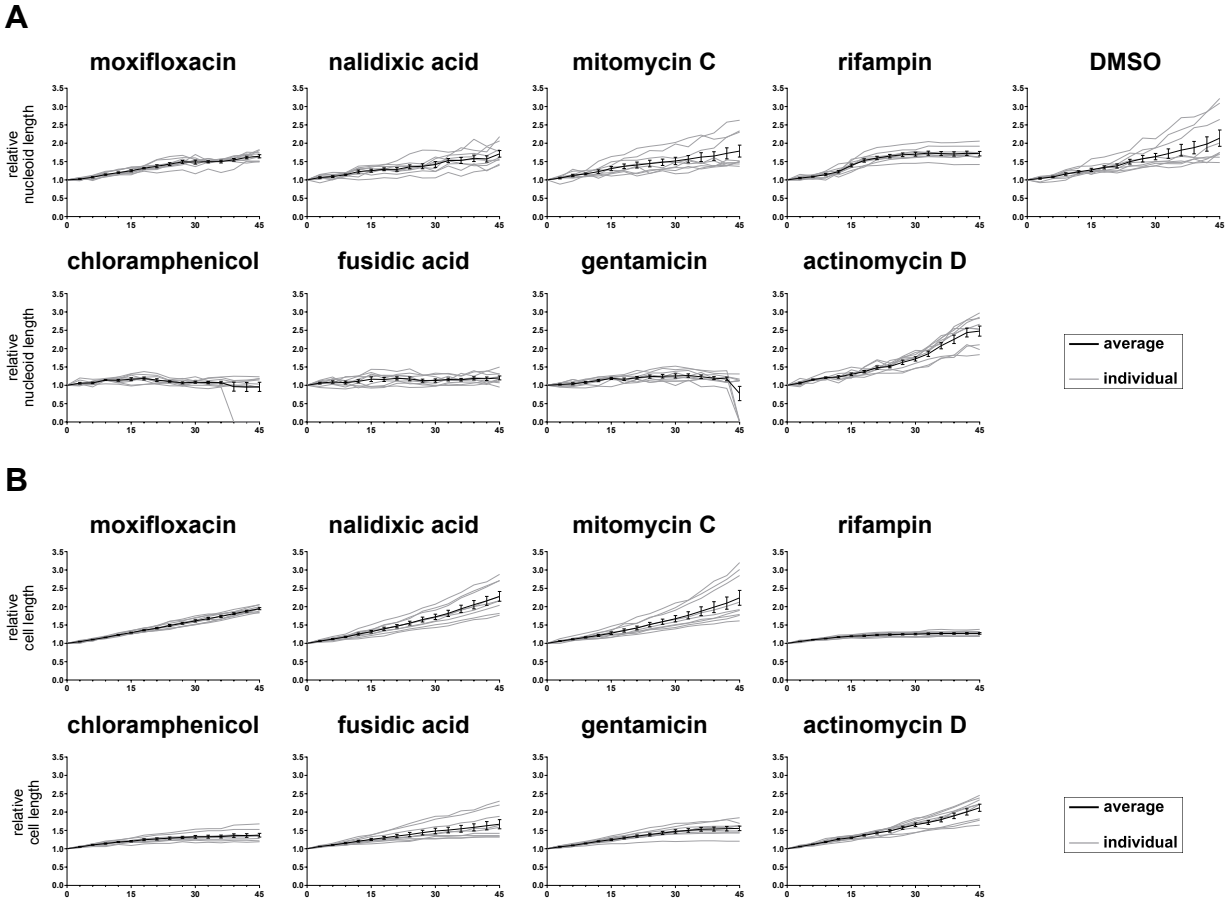
A
moxifloxacin
nalidixic acid
mitomycin C
rifampin
DMSO
chloramphenicol
fusidic acid
gentamicin
actinomycin D
relative nucleoid length
average
individual
B
moxifloxacin
nalidixic acid
mitomycin C
rifampin
chloramphenicol
fusidic acid
gentamicin
actinomycin D
relative cell length
average
individual

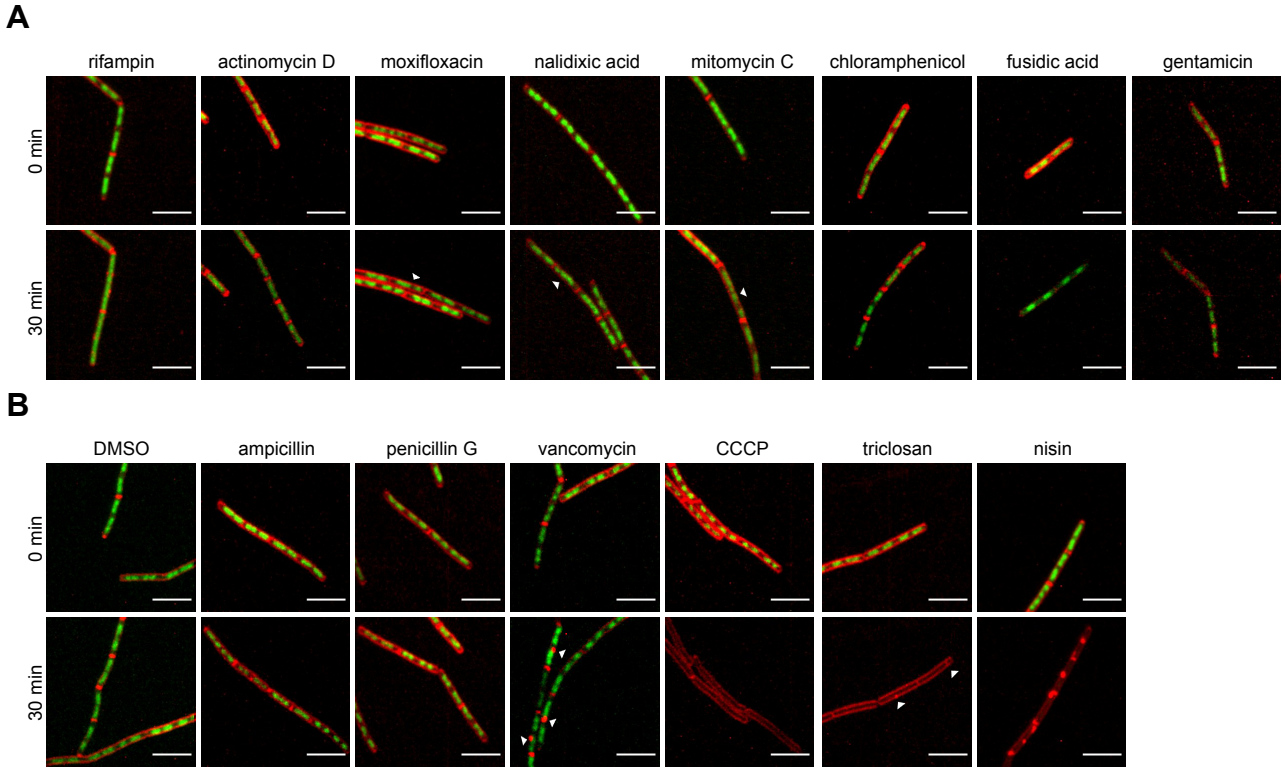
A
rifampin
actinomycin D
moxifloxacin
nalidixic acid
mitomycin C
chloramphenicol
fusidic acid
gentamicin
0 min
30 min
B
DMSO
ampicillin
penicillin G
vancomycin
CCCP
triclosan
nisin
0 min
30 min

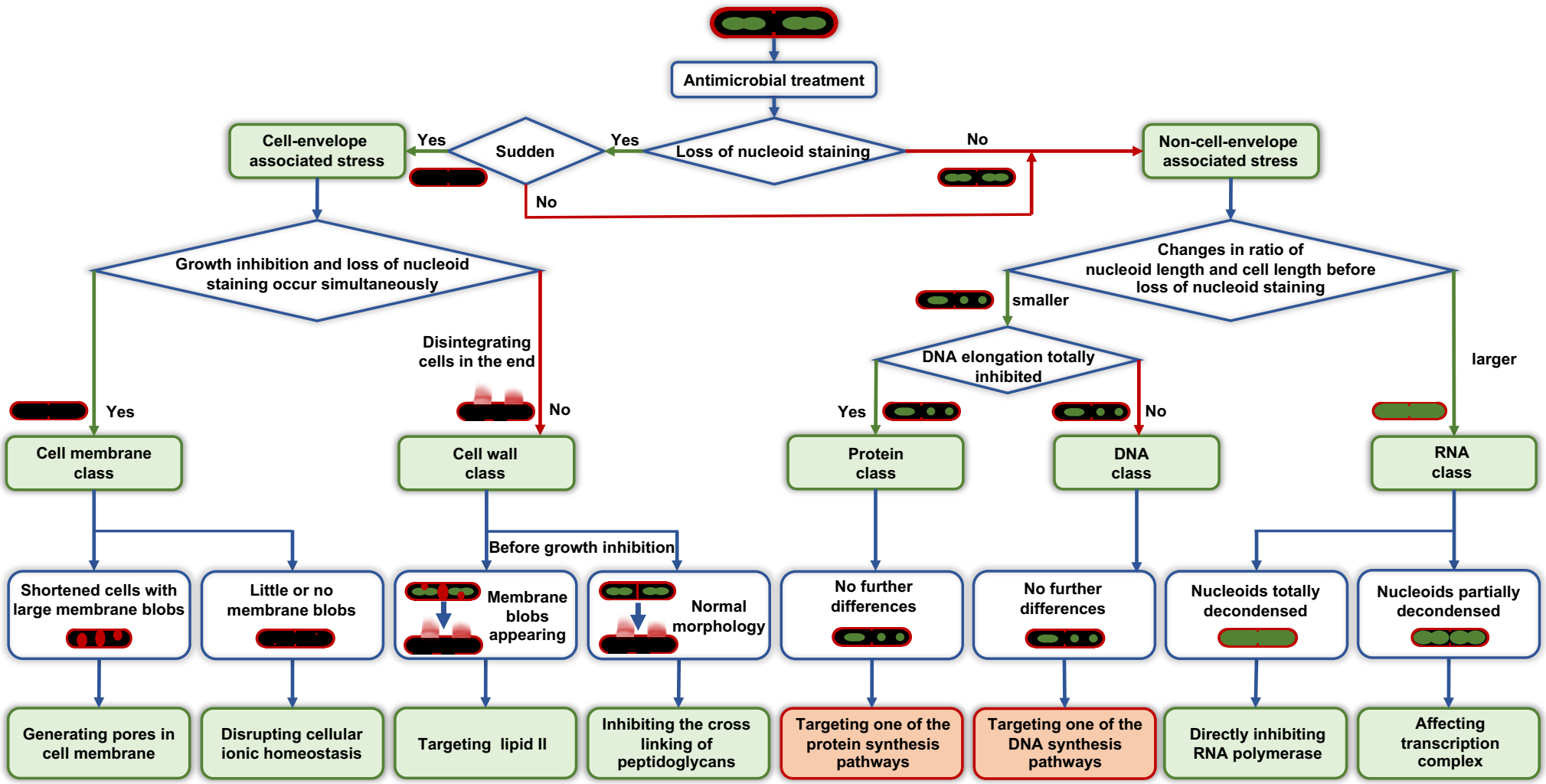
Antimicrobial treatment
Loss of nucleoid staining
Yes
Sudden
Yes
Cell-envelope associated stress
No
No
Non-cell-envelope associated stress
Growth inhibition and loss of nucleoid staining occur simultaneously
Yes
Disintegrating cells in the end
No
Changes in ratio of nucleoid length and cell length before loss of nucleoid staining
smaller
larger
DNA elongation totally inhibited
Yes
No
Cell membrane class
Cell wall class
Protein class
DNA class
RNA class
Before growth inhibition
Shortened cells with large membrane blobs
Little or no membrane blobs
Membrane blobs appearing
Normal morphology
No further differences
No further differences
Nucleoids totally decondensed
Nucleoids partially decondensed
Generating pores in cell membrane
Disrupting cellular ionic homeostasis
Targeting lipid II
Inhibiting the cross linking of peptidoglycans
Targeting one of the protein synthesis pathways
Targeting one of the DNA synthesis pathways
Directly inhibiting RNA polymerase
Affecting transcription complex

A

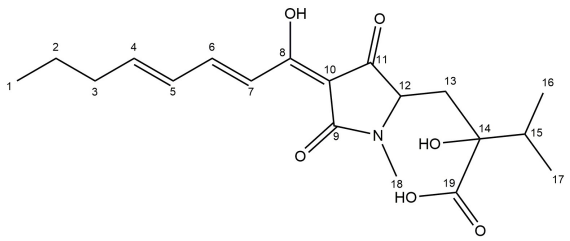
OH
O
HO
N
HO
O
O
1
2
3
4
5
6
7
8
9
10
11
12
13
14
15
16
17
18
19

B

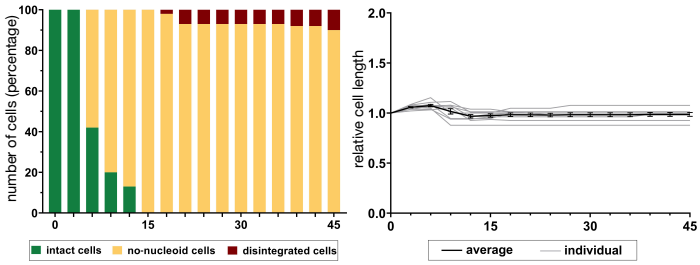
number of cells (percentage)
100
80
60
40
20
0
0
15
30
45
intact cells
no-nucleoid cells
disintegrated cells
relative cell length
2.0
1.5
1.0
0.5
0.0
average
individual

C

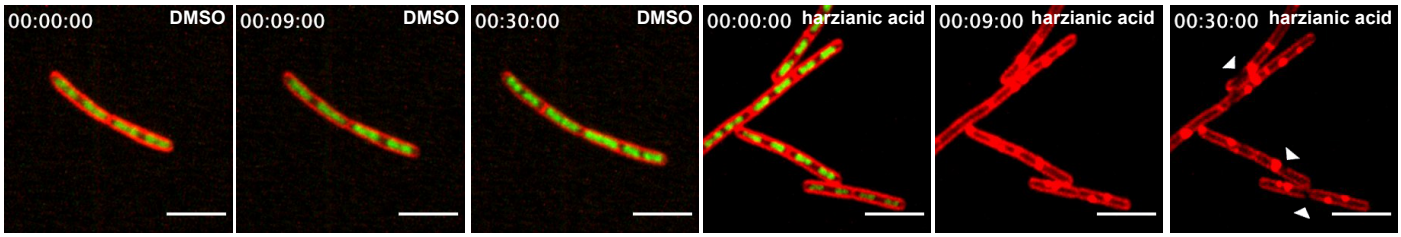
00:00:00 DMSO
00:09:00 DMSO
00:30:00 DMSO
00:00:00 harzianic acid
00:09:00 harzianic acid
00:30:00 harzianic acid

D

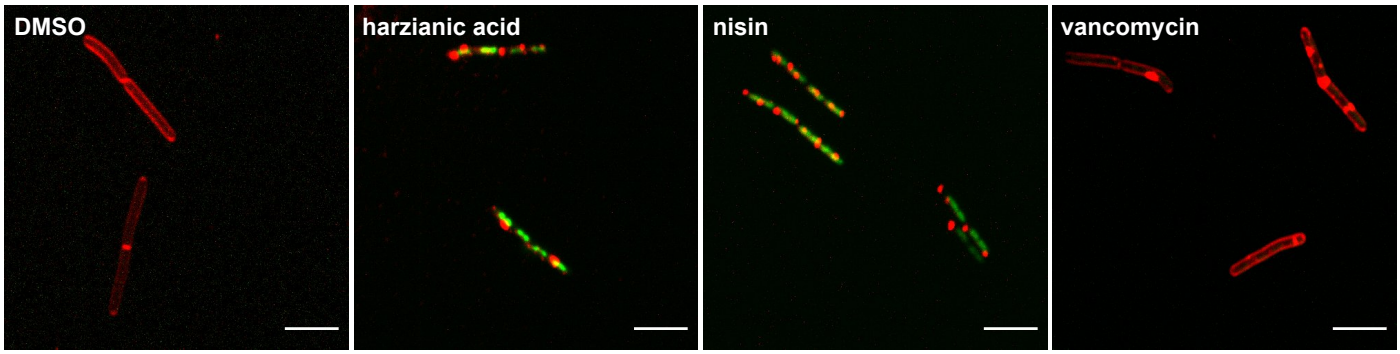
DMSO
harzianic acid
nisin
vancomycin